INORGANIC CHEMISTRY FRONTIERS

RESEARCH ARTICLE

View Article Online
View Journal | View Issue

Cite this: *Inorg. Chem. Front.*, 2025, **12**, 1040

Highly sensitive terbium-based metal–organic framework scintillators applied in flexible X-ray imaging†

Peng-Kun Wang,[a,b,c] Wen-Fei Wang,[a,b] Bao-Yi Li,[a,b,c] Rui-Xuan Qian,[a,b] Zhao-Xing Gao,[a,b] Shuai-Hua Wang, *[a,b,c] Fa-Kun Zheng *[a,b,c] and Guo-Cong Guo *[a,b,c]

Scintillators have played an indispensable role in public security and medical diagnosis fields due to their ability to convert X-ray photons into visible light. Metal–organic frameworks (MOFs) have the advantages of designable structures, easy preparation of flexible films and high stability, and hence show great potential in the field of scintillation. However, research on flexible X-ray imaging based on MOF scintillators has been rather limited. The exploration and development of MOF-based flexible scintillation screens would be very promising and exciting. Here, a novel terbium-based MOF (**Tb-MOF-1**) scintillator was synthesized and employed for X-ray detection and imaging. Benefiting from the sensitizing effect of the ligand, **Tb-MOF-1** shows excellent photoluminescence and radioluminescence signals, and its scintillation sensitivity is much higher than that of the commercial scintillator $Bi_4Ge_3O_{12}$ (BGO). **Tb-MOF-1** shows a low X-ray detection limit of 1.71 μGy s^{-1}, which is lower than the demand for medical diagnosis of 5.5 μGy s^{-1}. The scintillation mechanism of **Tb-MOF-1** is substantiated using spectroscopy and theoretical calculations. Furthermore, the robust structure of **Tb-MOF-1** brings its strong tolerance against water and X-ray dosages, which facilitates its long-term operation. A flexible scintillation screen (**Tb-MOF-screen**) derived from **Tb-MOF-1** was fabricated, achieving a high spatial resolution of 7.7 lp mm^{-1}@MTF 0.2. Ultimately, flexible X-ray imaging tests were successfully carried out by tightly fitting the **Tb-MOF-screen** to different curvature radii wires, which firstly verifies the X-ray imaging potential of Ln-MOF-based scintillation screens for non-planar objects.

Received 29th October 2024,
Accepted 13th December 2024

DOI: 10.1039/d4qi02736a

rsc.li/frontiers-inorganic

Introduction

Scintillators, which can convert X-ray photons into visible light, are the core of X-ray imaging technology and have been widely used in medical diagnostics, security inspections, industrial flaw detection, and other applications.[1–3] Although various scintillators have been employed for X-ray detection and imaging, many constraints remain, limiting their broader applications.[4–7] Inorganic scintillators require harsh conditions and costly equipment for their synthesis and their rigid nature hinders the realization of flexible X-ray imaging.[8] Organic scintillators show the merits of low production cost, good solubility and ease of processing into flexible films, but their inherently light elemental composition results in limited radioluminescence (RL) intensity and insufficient X-ray absorption ability.[9–11] Perovskite scintillators exhibit desirable comprehensive performance, but their instability to water or oxygen restricts their practical application.[12,13] To meet the demands of economic rationality, use feasibility and changeable environments, it is imperative to develop novel scintillators that simultaneously integrate the properties of easy preparation of flexible scintillation screens, strong X-ray absorbance and high stability.

Metal–organic frameworks (MOFs) have the advantages of designable structures, mild synthesis conditions and controllable manufacture of flexible devices, and hence show great potential in the field of scintillation.[14–16] The scintillation MOFs constructed with Pb^{2+}, Ba^{2+}, Zr^{4+} or Sr^{2+} show their RL properties derived from ligand luminescence, which can only display relatively limited scintillation intensities and sensitivities.[17–20] In contrast, the lanthanide-based MOFs (Ln-MOFs) have been considered as ideal scintillation candidate

[a]*State Key Laboratory of Structural Chemistry, Fujian Institute of Research on the Structure of Matter, Chinese Academy of Sciences, Fuzhou, Fujian 350002, P. R. China. E-mail: zfk@fjirsm.ac.cn*
[b]*Fujian Science & Technology Innovation Laboratory for Optoelectronic Information of China, Fuzhou, Fujian 350108, P. R. China*
[c]*University of Chinese Academy of Sciences, Beijing 100049, P. R. China*

†Electronic supplementary information (ESI) available: Radioluminescence spectra, FT-IR spectra and powder XRD pattern of **Tb-MOF-1**. CCDC 2346454 for **Tb-MOF-1**. For ESI and crystallographic data in CIF or other electronic format see DOI: https://doi.org/10.1039/d4qi02736a

materials that offer the possibility of realizing highly sensitive X-ray detection and imaging.[21,22] Specifically, the heavy lanthanide ions not only could absorb X-rays effectively, but also exhibit intrinsic lanthanide-centered luminescence characterized by narrow-band emission, high intensity, and a large Stokes shift.[23] The organic ligand not only sensitizes the luminescence of rare-earth ions but also confers excellent compatibility with polymer materials to lanthanide MOFs, laying the groundwork for the subsequent fabrication of flexible scintillation screens. Although several MOF-based flexible scintillation screens have been reported, research focusing on their application for flexible X-ray imaging is still limited.[23–25] To date, there is only one strontium-based MOF scintillation screen that has successfully achieved X-ray flexible imaging on curved wires with different curvatures.[20] Therefore, there is an urgent need to fill the huge gap in the flexible X-ray imaging field by preparing flexible scintillation screens with Ln-MOFs that combine strong luminescence and high stability to further validate their practical application potential.

Herein, a new scintillation Ln-MOF [Tb(HDOBPDC)(DMF)(H_2O)]$_n$ (**Tb-MOF-1**) was synthesized by a simple solvothermal method. The lanthanide terbium was chosen as the X-ray absorbing component and the luminescence center. The 3,3′-dihydroxy-4,4′-biphenyldicarboxylic acid (H_4DOBPDC), possessing strong coordination ability and sensitizing the lanthanide-centered luminescence, was selected as the organic ligand.[20,26] By synergizing the strong X-ray absorption of heavy Tb^{3+} ions with the excellent sensitization effect of organic ligands, **Tb-MOF-1** exhibits prominent Tb-based characteristic photoluminescence (PL) and RL properties as expected, and its X-ray detection sensitivity is higher than those of commercial scintillators $Bi_4Ge_3O_{12}$ (BGO), BaF_2, and our previously reported Sr-SMOF.[20] Notably, the RL mechanism of **Tb-MOF-1** was illustrated with the aid of spectroscopy and theoretical calculations. The detection limit of **Tb-MOF-1** is 1.71 μGy s^{-1}, which is lower than the requirement for X-ray medical diagnosis of 5.5 μGy s^{-1}. The scintillation performance of **Tb-MOF-1** shows no significant decrease after water immersion or high X-ray dosage irradiation, which ensures its long-term stable operation. Furthermore, a flexible scintillation screen (**Tb-MOF-screen**) with excellent stability was prepared by incorporating scintillator microcrystals into polydimethylsiloxane (PDMS), which achieves a high spatial resolution of 7.7 lp mm^{-1}@MTF 0.2. Eventually, the flexible X-ray imaging measurement for the bent wires in different directions was successfully realized by rotating the objective table.

Experimental section

Materials and synthesis

All reagents and solvents for synthesis and analysis were commercially available and used without further purification. A mixture of $Tb(NO_3)_3{\cdot}6H_2O$ (45.4 mg, 0.1 mmol), H_4DOBPDC (29.8 mg, 0.1 mmol), *N*,*N*′-dimethylformamide (DMF) (3 mL), deionized water (1 mL) and HBr acid (30 μL) was loaded into the 10 mL vial, which was sealed and heated to 120 °C for 2 d and then cooled to room temperature under ambient conditions to obtain colorless transparent rod-shaped crystals. Yield: about 53% based on Tb. Anal. calcd (%) for $C_{17}H_{16}N_1O_8Tb_1$: C 39.17, H 3.09, N 2.69. Found (%): C 39.08, H 2.80, N 2.89.

Physical characterization

Single-crystal X-ray diffraction data of **Tb-MOF-1** were obtained using a Rigaku FR-X Microfocus diffractometer equipped with a graphite-monochromated Mo K_α radiation (λ = 0.71073 Å) at room temperature.[27] The structure was solved by direct methods and refined using full-matrix least-squares on F^2 with Olex2 1.5 software. The hydrogen atoms were calculated in idealized positions and refined with a riding model.[28] All non-hydrogen atoms were refined anisotropically. Pertinent crystal data and structure refinement details for **Tb-MOF-1** are summarized in Table S1† and the selected bond lengths and bond angles were given in Table S2.† Powder X-ray diffraction (PXRD) patterns were collected on a Rigaku Miniflex 600 diffractometer using Cu K_α radiation (λ = 1.5406 Å) in the 2θ range of 5–65°. The FT-IR spectra were collected on a VERTEX 70 spectrometer using KBr pellets in the range of 4000–400 cm^{-1}. Elemental analyses (C, H, and N) were performed on an Elementar Vario EL III micro-analyzer. The photoluminescence (PL) spectra, luminescence lifetimes, and photoluminescence quantum yield (PLQY) tests were carried out on an Edinburgh FLS1000 UV/Vis/NIR fluorescence spectrometer.[29] The PLQY data were acquired using the 'Direct & Indirect Excitation' measurement method. The radioluminescence spectra, radiation luminescence stability, and X-ray sensitivity were collected on a self-built X-ray stimulated Edinburgh FLS920 fluorescence spectrometer (W target, 5 W). The samples were placed compactly in a quartz-capped copper plate with a certain volume, and the thickness of the sample tank was 2 mm. The spot of the X-ray and the fibre optic spectrometer can completely cover the samples. The fibre optic spectrometer was then used to collect emission spectra with excitation by X-rays. A lead box serves as an X-ray protective device. The detection limit tests were performed by recording the signal-to-noise ratio of scintillation intensity at different X-ray dose rates. The X-ray dose rate was attenuated by placing an aluminum plate in front of the X-ray source during the detection limit measurements. The X-ray images were acquired by using a digital camera (Canon 5D4) under 50 kV X-ray irradiation. The SEM images were recorded on a Zeiss Sigma 300 field emission scanning electron microscope. The used accelerating voltage is 1 kV. The simulated X-ray absorption spectra are obtained from the XCOM photon cross section database (**https://physics.nist.gov/PhysRefData/Xcom/html/xcom1.html**).[30]

Preparation of the Tb-MOF-screen

The crystals of **Tb-MOF-1** were ground and sieved into microcrystals with a size of less than 50 μm. The microcrystals of **Tb-MOF-1** (800 mg) were added to polydimethylsiloxane (PDMS) (1 mL) in a beaker. A homogeneous mixture was obtained by

stirring and sonication. The above mixed solution was evenly knife-coated onto a cleaned polyethylene terephthalate (PET) substrate and cured at room temperature to obtain the flexible **Tb-MOF-screen**.[11]

Calculation of electronic structures and density of states (DOS)

The calculation model of **Tb-MOF-1** was built directly from single-crystal X-ray diffraction data. Calculations of electronic structures and DOS were performed with DMol3 code based on DFT with the GGA-PBE functional in the Materials Studio v8.0 software package.[31]

Results and discussion

The **Tb-MOF-1** crystals were obtained by a simple solvothermal method. Structural analysis revealed that **Tb-MOF-1** crystallizes in the monoclinic space group $P2_1/c$, and its asymmetric unit comprises one Tb^{3+} ion, one ligand $HDOBPDC^{3-}$, one coordinating DMF molecule and a free water molecule (Fig. 1a). Each Tb^{3+} ion is coordinated to eight oxygen atoms from five $HDOBPDC^{3-}$ ligands and one DMF molecule to form a distorted dodecahedral configuration (Fig. S1†).

The $HDOBPDC^{3-}$ ligand adopts a μ_5-bridging mode with μ_2-η^1:η^1 and μ_3-η^2:η^2:η^1 styles to link Tb^{3+} ions within the Tb–O bond lengths of 2.213(4)–2.722(4) Å (Fig. S2†). The different Tb^{3+} centers were bridged *via* the oxygens from the carboxy and hydroxyl groups, generating a one-dimensional linear chain along the *a*-axis (Fig. S3a†), and the 1D chains are connected by the coordination of Tb^{3+} to the terminal carboxyl or hydroxyl oxygen atom of the ligand to form the 2D layer (Fig. S3b†), which further results in a 3D network by different ligands with large pore channels of 22.7 Å × 10.2 Å (Fig. S4† and Fig. 1b).

The purity and composition of the as-synthesized crystals **Tb-MOF-1** were confirmed by powdered X-ray diffraction (PXRD) (Fig. S5†), FT-IR spectroscopy (Fig. S6†), and elemental analyses.

The photoluminescence (PL) property of **Tb-MOF-1** was investigated firstly as a bright green light observed under ultraviolet (UV) light, which shows typical characteristic emission peaks of Tb^{3+} ions around 488 nm, 547 nm, 584 nm and 622 nm ($^5D_4 \rightarrow {}^7F_6$, $^5D_4 \rightarrow {}^7F_5$, $^5D_4 \rightarrow {}^7F_4$, $^5D_4 \rightarrow {}^7F_3$, respectively) (Fig. 2a),[32,33] obtaining the CIE coordinates (0.307, 0.597) (Fig. S7†).[25] The large Stokes shift between the excitation and emission spectra indicates slight self-absorption, which facilitates the realization of high scintillation intensity (Fig. S8†).[34,35] Moreover, the PL emission peaks of **Tb-MOF-1** remain almost constant with the variation of excitation wavelengths (Fig. S9†). It is noteworthy that the ligand $HDOBPDC^{3-}$ exhibits bright blue emissions under UV light, whereas there is almost no ligand-based luminescence observed in **Tb-MOF-1** (Fig. S10†). This suggests that the ligand $HDOBPDC^{3-}$ acts as energy transfer bridges to effectively sensitize the metal-centered luminescence. The PL decay lifetime of **Tb-MOF-1** was obtained (λ_{ex} = 399 nm, λ_{em} = 546 nm) as 78.81 μs, and such relatively rapid fluorescence decay lifetime would ensure a fast decay of the scintillation intensity, which facilitates the reduction of the scintillation afterglow (Fig. S11†). The PLQY of **Tb-MOF-1** is 11.04%, indicating a relatively strong photoluminescence ability (Fig. S12†).

The X-ray absorption spectra and thickness-dependent X-ray attenuation efficiency of **Tb-MOF-1** and some commercial scintillators were simulated to understand the potential to interact with X-rays, revealing that **Tb-MOF-1** demonstrates a favourable X-ray absorption and blocking capacity (Fig. 2b and S13†).[36] Benefiting from the commendable photoluminescence properties and strong X-ray absorption, **Tb-MOF-1** shows outstanding radioluminescence (RL) properties under X-rays (Fig. S14†), and its RL intensity shows a favorable dependence on the X-ray dose rates (Fig. S15†). It is noteworthy that the RL spectra of **Tb-MOF-1** exhibit identical peak shape and position to its PL spectra (Fig. 2c), which means that the RL and PL originate from the same terbium-based emission process.

The RL intensities of the reactants including the ligand, $Tb(NO_3)_3(H_2O)_6$, and their equimolar physical mixture (Mixture) were recorded under the same dose rate of 42.29 mGy s^{-1} to eliminate possible effects on scintillation, while they all displayed rather weak signals (Fig. 2d). These results emphasize that the formation of crystal structures combined the strong absorption of X-rays by the inorganic heavy metal Tb with the sensitization effect of organic ligands which is the essential prerequisite for the realization of the high RL signals of **Tb-MOF-1**.[37]

Thus, **Tb-MOF-1** scintillation should be generated according to the following processes: firstly, the heavy atoms of Tb^{3+} interact with X-ray photons to produce numerous high-energy electrons through photoelectric effects. Next, these high-energy thermal electrons further interact with the ligand $HDOBPDC^{3-}$ by Compton scattering and lose energy, and the ligands are ionized and excited simultaneously to the excited triplet (T_1) states. Ultimately, the energy transfer from the T_1 state of $HDOBPDC^{3-}$ to Tb^{3+} occurred effectively, which led to the Tb-based characteristic emissions (Fig. 2e).[38]

The total and partial densities of states of **Tb-MOF-1** were calculated to further elucidate the X-ray-induced RL mechanism. The ligand $HDOBPDC^{3-}$ contributes significantly to

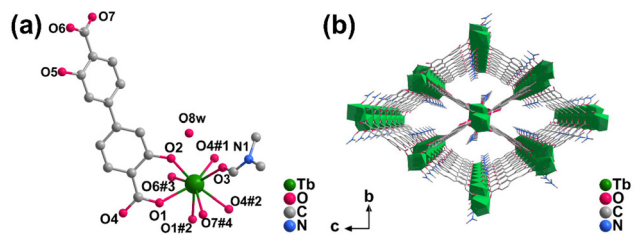

Fig. 1 (a) The asymmetric unit of **Tb-MOF-1**. (b) The 3D frame aggregation along the *a*-axis of **Tb-MOF-1**. All hydrogen atoms and free water molecules are omitted for clarity. Symmetry codes: #1 1 + *x*, *y*, *z*; #2 1 – *x*, –*y*, 1 – *z*; #3 1 – *x*, –1/2 + *y*, 1/2 – *z*; #4 *x*, 1/2 – *y*, 1/2 + *z*.

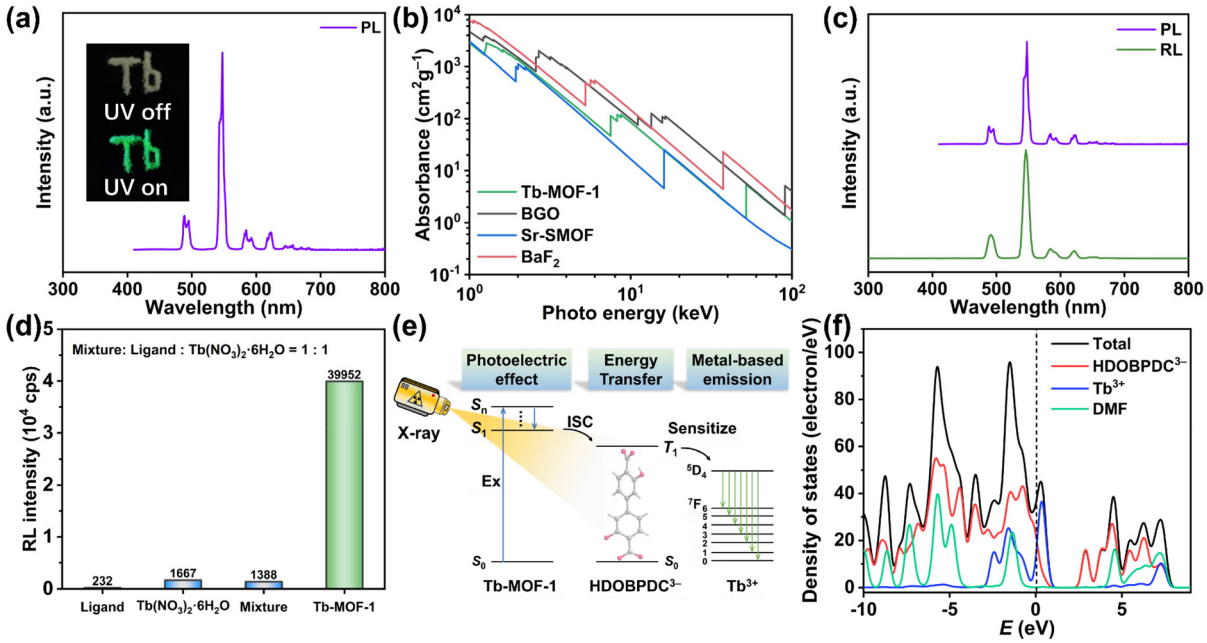

Fig. 2 (a) The PL spectra of **Tb-MOF-1**. The inset shows the photographs of crystals of **Tb-MOF-1** under natural light and UV light, respectively. (b) The simulated X-ray absorption spectra of **Tb-MOF-1**, BGO, Sr-SMOF,[16] and BaF_2 as a function of the X-ray energy ranging from 1 to 100 keV. (c) The PL and RL spectra of **Tb-MOF-1**. (d) The RL intensity of raw reactants, including the ligand, $Tb(NO_3)_3(H_2O)_6$, the equimolar physical mixture (Mixture) and **Tb-MOF-1** under the same dose rate of 42.29 mGy s^{-1}. (e) Diagram of the RL mechanism of **Tb-MOF-1**. (f) The profile of the total/partial electronic density of states of **Tb-MOF-1**.

both the valence band maximum (VBM) and conduction band minimum (CBM) (Fig. 2f), and the Tb^{3+} ion has a prominent contribution from its f orbital at the VBM and its d orbital at the CBM, which may correspond to its $^5D_4 \rightarrow {}^7F_n$ radiation transition behaviors (Fig. S16†). Notably, the high-energy X-ray can excite the deep-energy-level electrons of heavy metals, whereas the p orbital electrons from Tb^{3+} ions precisely contribute prominently to the deep valence band in the energy range from −17.08 to −15.17 eV (Fig. S16†). The theoretical calculations further reveal that the scintillation process of **Tb-MOF-1** could originate from the metals absorbing X-rays, inducing ligand-sensitized Tb^{3+} ion radioluminescence through energy transfer.

The RL spectra of **Tb-MOF-1**, BGO, Sr-SMOF,[20] and BaF_2 were measured at the same dose rate of 42.29 mGy s^{-1} to further compare their scintillation performance, and the RL intensity of **Tb-MOF-1** is much higher than those of other scintillators (Fig. 3a). To better characterize the X-ray detection performance of scintillators, the linear relationship between RL intensity and X-ray dose rates of **Tb-MOF-1**, BGO, BaF_2, and Sr-SMOF was recorded. Specifically, **Tb-MOF-1** manifests a higher slope than BGO, BaF_2 and Sr-SMOF, implying a more efficient X-ray response sensitivity (Fig. 3b). The detection limit was calculated to be 1.71 μGy s^{-1} by the linear relationship between the low dose rates and RL signal-to-noise ratios, which satisfies the demand of X-ray medical diagnostics (5.5 μGy s^{-1}) (Fig. 3c).[39] Nevertheless, the detection limit of BaF_2 was as high as 2.76 mGy s^{-1} (Fig. S17†). The comparison of some commercial scintillators of CsI:Tl, Gd_2O_2S:Tb and BaF_2 shows that **Tb-MOF-1** displays a good comprehensive performance (Table S3†).

The stability of the scintillator is a non-negligible indicator of the realization of its practical application.[40,41] The dose-dependent RL intensity results revealed that **Tb-MOF-1** maintained its favorable performance after irradiation at a relatively high X-ray dose rate of 42.29 mGy s^{-1} for 3 h with a cumulative dose of 457 Gy (Fig. 3d). The PXRD results further verified that **Tb-MOF-1** had not undergone structural changes or collapse after continuous X-ray irradiation (Fig. S18†). The fatigue resistance test reveals that **Tb-MOF-1** shows favorable performance retention after 230 times on/off operations at an irradiation dose of 42.29 mGy s^{-1} (Fig. 3e). After being immersed in water for 30 d, the RL sensitivity of **Tb-MOF-1** was nearly maintained (Fig. 3f), and its crystal structure remained unchanged (Fig. S19†). The stability test results indicate that **Tb-MOF-1** shows a remarkable ability to tolerate radiation dose and water degradation, which is conducive to its long-term stable operation.[42]

The high sensitivity and stability of **Tb-MOF-1** prompted us to prepare scintillation screens to realize X-ray imaging. The mixture of **Tb-MOF-1** microcrystals and PDMS was knife-coated on the polyethylene terephthalate (PET) substrate to obtain a flat scintillation screen (**Tb-MOF-screen**) with excellent flexibility and a bright green light under UV light (Fig. 4a and S20†),[43] which was also found to have superior homogeneity from scanning electron microscopy (SEM) results (Fig. S21†). The RL intensity of the **Tb-MOF-screen** also dis-

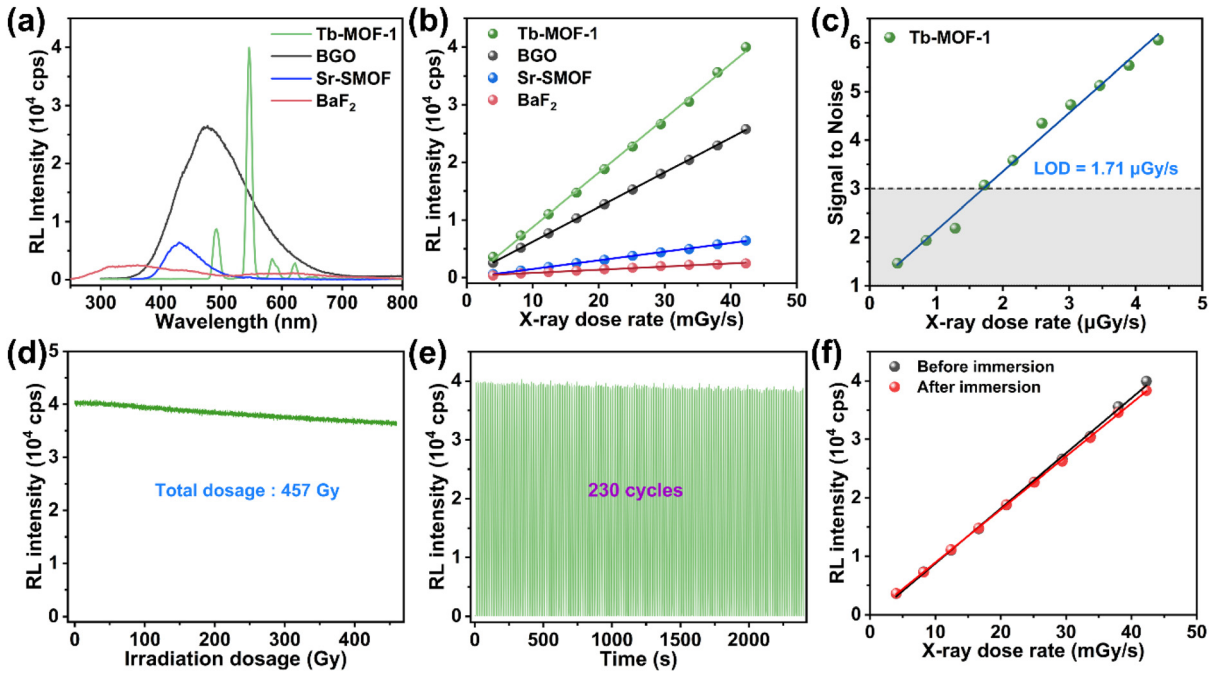

Fig. 3 (a) RL spectra of **Tb-MOF-1**, BGO, Sr-SMOF and BaF_2. (b) X-ray detection sensitivity of **Tb-MOF-1**, BGO, Sr-SMOF and BaF_2. (c) The detection limit of **Tb-MOF-1**. (d) Radiation stability of **Tb-MOF-1** under continuous X-ray irradiation at a dose rate of 42.29 mGy s^{-1} for 3 h. (e) RL intensities recorded for **Tb-MOF-1** over continuous 230 on/off cycles (dose rate: 42.29 mGy s^{-1}). (f) The sensitivities of **Tb-MOF-1** before and after being immersed in water for 30 d.

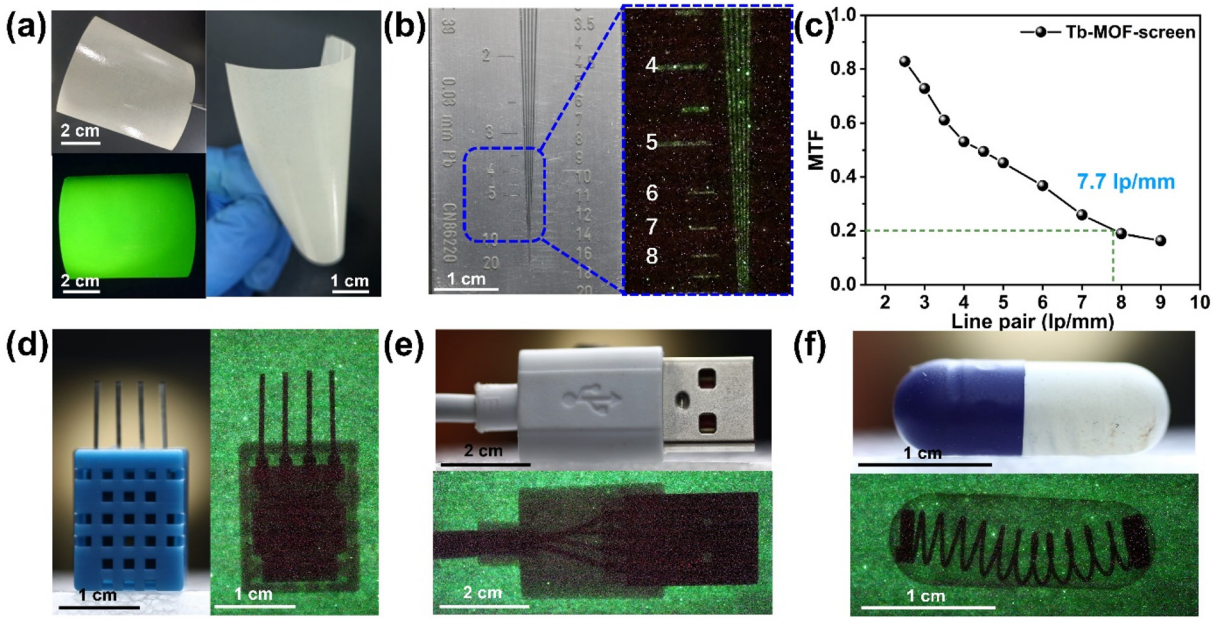

Fig. 4 (a) The photographs of the flexible **Tb-MOF-screen**. (b) Profile displays (left) and X-ray images (right) of the standard line pair card. (c) MTF of the X-ray image based on the standard line pair card. The real pictures and X-ray radiographs of the electronic component (d), the USB connector (e), and the capsule (f).

plays an outstanding linear relationship with the X-ray dose rates (Fig. S22 and S23†). The **Tb-MOF-screen** also exhibits a favourable irradiation and fatigue resistance (Fig. S24†).

To validate the X-ray imaging capability of the **Tb-MOF-screen**, a simple imaging system was built to find the internal structures of different objects (Fig. S25†). The modulation

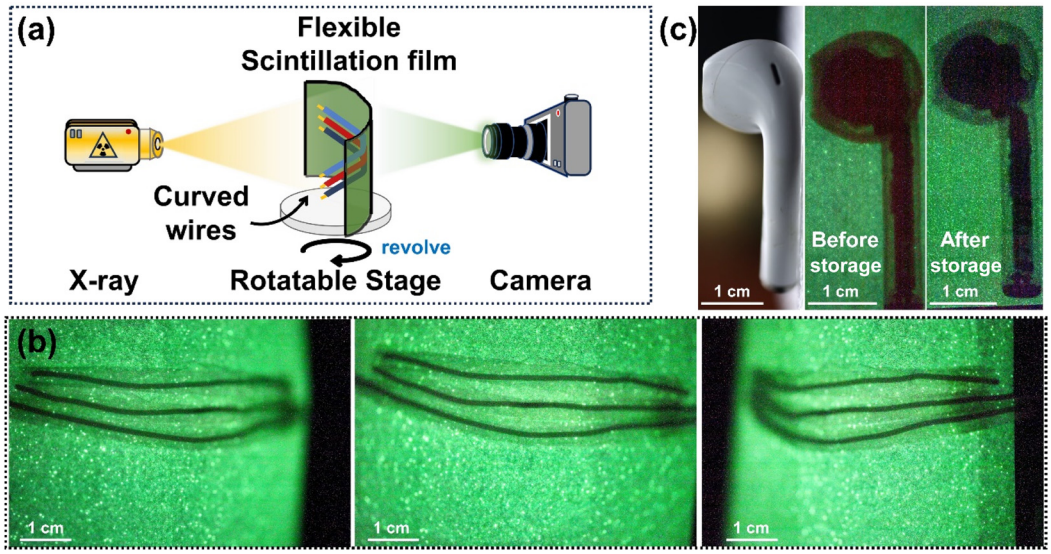

Fig. 5 (a) Schematic diagram of the flexible X-ray imaging system. (b) The X-ray radiographs of the flexible **Tb-MOF-screen** for curved wires (45°) with different directions. (c) The physical photograph and X-ray radiograph of the **Tb-MOF-screen** for the airpot before and after being stored for 60 d under ambient conditions (20–38 °C, 40–65% humidity).

transfer function (MTF) at different spatial resolutions was obtained and calculated by X-ray imaging of a standard line pair card (Fig. 4b).[44]

The spatial resolution of the **Tb-MOF-screen** is 7.7 lp mm^{-1} when the MTF value is 0.2 (Fig. 4c), which is higher than those of the commercial CsI:Tl, Gd_2O_2S:Tb or α-Se flat panel detectors (≈5 lp mm^{-1} at MTF 0.2) (Table S3†).[2,45] Moreover, the internal structure of the electronic component or USB connector and the spring in the capsule are all clearly identifiable, and both are completely invisible to the naked eye in natural light (Fig. 4d–f and S26†). These results suggest that the **Tb-MOF-screen** has a favorable X-ray imaging capability.

The flexible X-ray imaging tests were conducted to verify the application potential for non-destructive detection of the **Tb-MOF-screen** for bent objects.[46] The internal structural information of the bent wires was recorded on the **Tb-MOF-screen** at different angles by simultaneously rotating the bent wire and the flexible screen (Fig. 5a, S27 and S28†). Specifically, the flexible **Tb-MOF-screen** could reduce image distortion by tightly fitting the curved wires with different curvature radii, which could obtain clearly visible imaging photographs in different directions (Fig. 5b and S29†).[47] After being stored for 60 d under ambient conditions (20–38 °C, 30–65% humidity), the **Tb-MOF-screen** could maintain its high-quality X-ray radiograph, validating its high stability against heat, humidity and oxygen degradation (Fig. 5c).

Conclusions

In summary, a novel terbium-based metal–organic framework (**Tb-MOF-1**) was synthesized and applied in X-ray scintillation imaging successfully. Benefitting from the sensitizing effect from the ligand $HDOBPDC^{3-}$, **Tb-MOF-1** shows favorable Tb^{3+}-based PL and RL signals, which achieves a higher scintillation sensitivity than the commercial scintillator BGO. A low detection limit of 1.71 μGy s^{-1} was obtained, satisfying the typical X-ray medical diagnostic requirement of 5.5 μGy s^{-1}. Simultaneously, the scintillation mechanism of **Tb-MOF-1** was elucidated with the support of spectroscopy and theoretical calculations. Owing to its robust structure, **Tb-MOF-1** exhibits strong stability against water and high X-ray dosages. Moreover, a flexible scintillation screen (**Tb-MOF-screen**) was prepared with PDMS, achieving a high resolution of 7.7 lp mm^{-1}@MTF 0.2, which is higher than those of commercial CsI:Tl or α-Se flat panel detectors. Additionally, the flexible X-ray imaging tests for curved objects with different curvature radii have been successfully realized by simultaneously rotating the wires and the flexible screen. This work provides a new candidate scintillator for X-ray detection and verifies the potential of Ln-MOFs applied for flexible X-ray imaging for the first time.

Author contributions

Peng-Kun Wang designed and synthesized compounds, and wrote the draft. Wen-Fei Wang assisted in crystal structure analysis and analyzed experimental results. Bao-Yi Li, Rui-Xuan Qian and Zhao-Xing Gao assisted in testing. Shuai-Hua Wang assisted in the DFT calculations and revised the manuscript. Fa-Kun Zheng conceived the experiments, analyzed and discussed the results, and revised the manuscript. Guo-Cong Guo revised the manuscript. All the authors have approved the final version of the manuscript.

Data availability

The data that support the findings of this study are available on request from the corresponding author.

Conflicts of interest

The authors declare that they have no known competing financial interests or personal relationships that could have appeared to influence the work reported in this paper.

Acknowledgements

This work was financially supported by the National Natural Science Foundation of China (21971240 and 22271283) and the Scientific Instrument Developing Project of the Chinese Academy of Sciences (YJKYYQ20210039). We sincerely thank Prof. Shao-Fan Wu from Fujian Institute of Research on the Structure of Matter, Chinese Academy of Sciences, for the help with measurements.

References

1 H. Wu, Q. Wang, A. Zhang, G. Niu, M. Nikl, C. Ming, J. Zhu, Z. Zhou, Y.-Y. Sun, G. Nan, G. Ren, Y. Wu and J. Tang, One-dimensional Scintillator Film with Benign Grain Boundaries for High-Resolution and Fast X-ray Imaging, *Sci. Adv.*, 2023, **9**, eadh1789.

2 L. Yang, Z. Li, L. He, J. Sun, J. Wang, Y. Wang, M. Li, Z. Zhu, X. Dai, S. Hu, F. Zhai, Q. Yang, Y. Tao, Z. Chai, S. Wang and Y. Wang, Emergence of a Lanthanide Chalcogenide as an Ideal Scintillator for a Flexible X–ray Detector, *Angew. Chem., Int. Ed.*, 2023, e202306465.

3 T. Wang, S. Hu, T. Ji, X. Zhu, G. Zeng, L. Huang, A. N. Yakovlev, J. Qiu, X. Xu and X. Yu, High–temperature X–ray Imaging with Transparent Ceramics Scintillators, *Laser Photonics Rev.*, 2024, 2300892.

4 X. Ou, X. Qin, B. Huang, J. Zan, Q. Wu, Z. Hong, L. Xie, H. Bian, Z. Yi, X. Chen, Y. Wu, X. Song, J. Li, Q. Chen, H. Yang and X. Liu, High-Resolution X-ray Luminescence Extension Imaging, *Nature*, 2021, **590**, 410–415.

5 Z. Li, G. Peng, Z. Li, Y. Xu, T. Wang, H. Wang, Z. Liu, G. Wang, L. Ding and Z. Jin, Hydrogen Bonds Strengthened Metal–Free Perovskite for Degradable X–ray Detector with Enhanced Stability, Flexibility and Sensitivity, *Angew. Chem., Int. Ed.*, 2023, **62**, e202218349.

6 F. Zhang, Y. Zhou, Z. Chen, M. Wang, Z. Ma, X. Chen, M. Jia, D. Wu, J. Xiao, X. Li, Y. Zhang, Z. Shi and C. Shan, Thermally Activated Delayed Fluorescence Zirconium–Based Perovskites for Large–Area and Ultraflexible X–ray Scintillator Screens, *Adv. Mater.*, 2022, **34**, 2204801.

7 Y. Wang, X. Yin, W. Liu, J. Xie, J. Chen, M. A. Silver, D. Sheng, L. Chen, J. Diwu, N. Liu, Z. Chai, T. E. Albrecht-Schmitt and S. Wang, Emergence of Uranium as a Distinct Metal Center for Building Intrinsic X–ray Scintillators, *Angew. Chem., Int. Ed.*, 2018, **57**, 7883–7887.

8 X. Liu, R. Li, X. Xu, Y. Jiang, W. Zhu, Y. Yao, F. Li, X. Tao, S. Liu, W. Huang and Q. Zhao, Lanthanide(III)–Cu_4I_4 Organic Framework Scintillators Sensitized by Cluster–Based Antenna for High–Resolution X–ray Imaging, *Adv. Mater.*, 2023, **35**, 2206741.

9 J.-X. Wang, L. Gutiérrez-Arzaluz, X. Wang, M. Almalki, J. Yin, J. Czaban-Jóźwiak, O. Shekhah, Y. Zhang, O. M. Bakr, M. Eddaoudi and O. F. Mohammed, Nearly 100% Energy Transfer at the Interface of Metal-Organic Frameworks for X-ray Imaging Scintillators, *Matter*, 2022, **5**, 253–265.

10 X. Du, S. Zhao, L. Wang, H. Wu, F. Ye, K.-H. Xue, S. Peng, J. Xia, Z. Sang, D. Zhang, Z. Xiong, Z. Zheng, L. Xu, G. Niu and J. Tang, Efficient and ultrafast organic scintillators by hot exciton manipulation, *Nat. Photonics*, 2024, **18**, 162–169.

11 X. Wang, X. Wang, J. Song, H. Bao, M. Yuan, Y. Wang, L. Kong and W. Liu, Anchoring the AIEgen by Zr Clusters in Metal-Organic Gel for Efficient X-ray Detection and Imaging, *Chem*, 2024, **10**, 1268–1278.

12 T. He, Y. Zhou, P. Yuan, J. Yin, L. Gutiérrez-Arzaluz, S. Chen, J.-X. Wang, S. Thomas, H. N. Alshareef, O. M. Bakr and O. F. Mohammed, Copper Iodide Inks for High-Resolution X-ray Imaging Screens, *ACS Energy Lett.*, 2023, **8**, 1362–1370.

13 W.-F. Wang, M.-J. Xie, P.-K. Wang, J. Lu, B.-Y. Li, M.-S. Wang, S.-H. Wang, F.-K. Zheng and G.-C. Guo, Thermally Activated Delayed Fluorescence (TADF)–active Coinage–metal Sulfide Clusters for High–resolution X–ray Imaging, *Angew. Chem., Int. Ed.*, 2023, e202318026.

14 J. Perego, I. Villa, A. Pedrini, E. C. Padovani, R. Crapanzano, A. Vedda, C. Dujardin, C. X. Bezuidenhout, S. Bracco, P. E. Sozzani, A. Comotti, L. Gironi, M. Beretta, M. Salomoni, N. Kratochwil, S. Gundacker, E. Auffray, F. Meinardi and A. Monguzzi, Composite Fast Scintillators Based on High-Z Fluorescent Metal–Organic Framework Nanocrystals, *Nat. Photonics*, 2021, **15**, 393–400.

15 M. Orfano, J. Perego, C. X. Bezuidenhout, I. Villa, R. Lorenzi, B. Sabot, S. Pierre, S. Bracco, S. Piva, A. Comotti and A. Monguzzi, Reabsorption–Free Scintillating Hetero–Ligand MOF Crystals Activated by Ultrafast Energy Transfer, *Adv. Funct. Mater.*, 2024, 2404480.

16 H. Liu, H. Qin, N. Shen, S. Yan, Y. Wang, X. Yin, X. Chen, C. Zhang, X. Dai, R. Zhou, X. Ouyang, Z. Chai and S. Wang, Emergence of a Radical–Stabilizing Metal–Organic Framework as a Radio–photoluminescence Dosimeter, *Angew. Chem., Int. Ed.*, 2020, **59**, 15209–15214.

17 W.-F. Wang, J. Lu, X.-M. Xu, B.-Y. Li, J. Gao, M.-J. Xie, S.-H. Wang, F.-K. Zheng and G.-C. Guo, Sensitive X-ray Detection and Imaging by a Scintillating Lead(II)-Based Metal-Organic Framework, *Chem. Eng. J.*, 2022, **430**, 133010.

18 J. Lu, J. Gao, W.-F. Wang, B.-Y. Li, P.-X. Li, F.-K. Zheng and G.-C. Guo, Barium-based Scintillating MOFs for X-ray Dosage Detection with Intrinsic Energy Resolution via

Luminescent Multidentate Naphthalene Disulfonate Moieties, *J. Mater. Chem. C*, 2021, **9**, 5615–5620.

19 C. Wang, O. Volotskova, K. Lu, M. Ahmad, C. Sun, L. Xing and W. Lin, Synergistic Assembly of Heavy Metal Clusters and Luminescent Organic Bridging Ligands in Metal–Organic Frameworks for Highly Efficient X-ray Scintillation, *J. Am. Chem. Soc.*, 2014, **136**, 6171–6174.

20 P.-K. Wang, W.-F. Wang, B.-Y. Li, M.-J. Xie, H.-Y. Bian, S.-H. Wang, F.-K. Zheng and G.-C. Guo, Flexible Strontium-Based Metal–Organic Framework Scintillation Screens for High-Resolution X-ray Imaging, *Inorg. Chem. Front.*, 2023, **10**, 5710–5718.

21 F. P. Doty, C. A. Bauer, A. J. Skulan, P. G. Grant and M. D. Allendorf, Scintillating Metal–Organic Frameworks: A New Class of Radiation Detection Materials, *Adv. Mater.*, 2009, **21**, 95–101.

22 X. Wang, Y. Wang, Y. Wang, H. Liu, Y. Zhang, W. Liu, X. Wang and S. Wang, Color-Tunable X-ray Scintillation Based on a Series of Isotypic Lanthanide–Organic Frameworks, *Chem. Commun.*, 2020, **56**, 233–236.

23 X. Zhang, H. Qiu, W. Luo, K. Huang, Y. Chen, J. Zhang, B. Wang, D. Peng, Y. Wang and K. Zheng, High–Performance X–Ray Imaging using Lanthanide Metal–Organic Frameworks, *Adv. Sci.*, 2023, 2207004.

24 J. Gao, J. Lu, B. Li, W. Wang, M. Xie, S. Wang, F. Zheng and G. Guo, Illuminations for Constructions of Scintillating Lanthanide–Organic Complexes in Sensitive X-ray Detection and High-Resolution Radiative Imaging, *Chin. Chem. Lett.*, 2022, **33**, 5132–5136.

25 Z. Ajoyan, G. A. Mandl, P. R. Donnarumma, V. Quezada-Novoa, H. A. Bicalho, H. M. Titi, J. A. Capobianco and A. J. Howarth, Modulating Photo- and Radioluminescence in Tb(III) Cluster-Based Metal–Organic Frameworks, *ACS Mater. Lett.*, 2022, **4**, 1025–1031.

26 X. Liu, X. Wang, T. Gao, Y. Xu, X. Shen and D. Zhu, Three 3D Lanthanide–Organic Frameworks with Sra Topology: Syntheses, Structures, Luminescence and Magnetic Properties, *CrystEngComm*, 2014, **16**, 2779.

27 C. Dong, X. Song, B. E. Hasanov, Y. Yuan, L. Gutiérrez-Arzaluz, P. Yuan, S. Nematulloev, M. Bayindir, O. F. Mohammed and O. M. Bakr, Organic–Inorganic Hybrid Glasses of Atomically Precise Nanoclusters, *J. Am. Chem. Soc.*, 2024, **146**, 7373–7385.

28 G. Zhang, F. Chen, Y. Di, S. Yuan, Y. Zhang, X. Quan, Y. Chen, H. Chen and M. Lin, Guest–Induced Thermally Activated Delayed Fluorescence Organic Supramolcular Macrocycle Scintillators for High–Resolution X–Ray Imaging, *Adv. Funct. Mater.*, 2024, 2404123.

29 J. Luo, J. Wei, Z. Zhang, Z. He and D. Kuang, A Melt–Quenched Luminescent Glass of an Organic–Inorganic Manganese Halide as a Large–Area Scintillator for Radiation Detection, *Angew. Chem.*, 2023, **135**, e202216504.

30 A. Ciavatti, R. Sorrentino, L. Basiricò, B. Passarella, M. Caironi, A. Petrozza and B. Fraboni, High–Sensitivity Flexible X–Ray Detectors based on Printed Perovskite Inks, *Adv. Funct. Mater.*, 2021, **31**, 2009072.

31 M. C. Payne, M. P. Teter, D. C. Allan, T. A. Arias and J. D. Joannopoulos, Iterative minimization techniques for *ab initio* total-energy calculations: molecular dynamics and conjugate gradients, *Rev. Mod. Phys.*, 1992, **64**, 1045–1097.

32 H. Lu, M. Xu, J. Ma, J. Yang, Y. Bai, Z. Zhang, J. Qian, M. He, J. Wang and J. Lin, Constructing Lanthanide–Organic Complexes for X–ray Scintillation and Imaging, *Chem. – Eur. J.*, 2024, **30**, e202303918.

33 M. D. Allendorf, C. A. Bauer, R. K. Bhakta and R. J. T. Houk, Luminescent Metal–Organic Frameworks, *Chem. Soc. Rev.*, 2009, **38**, 1330.

34 J. Perego, C. X. Bezuidenhout, I. Villa, F. Cova, R. Crapanzano, I. Frank, F. Pagano, N. Kratochwill, E. Auffray, S. Bracco, A. Vedda, C. Dujardin, P. E. Sozzani, F. Meinardi, A. Comotti and A. Monguzzi, Highly Luminescent Scintillating Hetero-Ligand MOF Nanocrystals with Engineered Stokes Shift for Photonic Applications, *Nat. Commun.*, 2022, **13**, 3504.

35 B. M. Saidzhonov, K. E. Yorov, P. Yuan, S. Nematulloev, A. A. Karluk, T. Ahmad, O. F. Mohammed, O. M. Bakr and M. Bayindir, Multimaterial Fibers with Nanoemitters Enable Conformal X-ray Imaging with 3D Printed and Woven Scintillators, *ACS Mater. Lett.*, 2024, **6**, 1779–1789.

36 X. Zhou, K. Han, Y. Wang, J. Jin, S. Jiang, Q. Zhang and Z. Xia, Energy–Trapping Management in X–Ray Storage Phosphors for Flexible 3D Imaging, *Adv. Mater.*, 2023, **35**, 2212022.

37 H. Li, Y. Li, L. Zhang, E. Hu, D. Zhao, H. Guo and G. Qian, A Thermo–Responsive MOFs for X–Ray Scintillator, *Adv. Mater.*, 2024, 2405535.

38 D. Meng, T. Zhao, D. Busko, A. Cosgun Ergene, B. S. Richards and I. A. Howard, Tb and Eu in MOF–76: Elucidating the Mechanisms Responsible for the Divergent Excellent and Poor Photoluminescence Quantum Yields, *Adv. Opt. Mater.*, 2024, **12**, 2300867.

39 P.-K. Wang, W.-F. Wang, K.-B. Jiang, B.-Y. Li, S.-H. Wang, F.-K. Zheng and G.-C. Guo, Efficient X-ray Detection of Polyoxometalates@Metal–Organic Frameworks Based on Host–Guest Electron Transfer, *ACS Mater. Lett.*, 2024, **6**, 1086–1093.

40 Y.-H. Liu, N.-N. Wang, M.-P. Ren, X. Yan, Y.-F. Wu, C.-Y. Yue and X.-W. Lei, Zero-Dimensional Hybrid Cuprous Halide of [BAPMA]Cu_2Br_5 as a Highly Efficient Light Emitter and an X-Ray Scintillator, *ACS Appl. Mater. Interfaces*, 2023, **15**, 20219–20227.

41 Z. Wang, Y. Wei, C. Liu, Y. Liu and M. Hong, Mn^{2+}–Activated $Cs_3Cu_2I_5$ Nano–Scintillators for Ultra–High Resolution Flexible X–Ray Imaging, *Laser Photonics Rev.*, 2023, **17**, 2200851.

42 J.-W. Yuan, Q.-C. Peng, J.-C. Fu, Q. Yang, Z.-Y. Gao, Z.-Y. Wang, K. Li, S.-Q. Zang and B. Z. Tang, Highly Efficient Stable Luminescent Radical-Based X-ray Scintillator, *J. Am. Chem. Soc.*, 2023, **145**, 27095–27102.

43 L.-J. Xu, X. Lin, Q. He, M. Worku and B. Ma, Highly Efficient Eco-Friendly X-ray Scintillators Based on an Organic Manganese Halide, *Nat. Commun.*, 2020, **11**, 4329.

44 V. Naresh, P.-R. Cha and N. Lee, $Cs_2NaGdCl_6:Tb^{3+}$–A Highly Luminescent Rare-Earth Double Perovskite Scintillator for Low-Dose X-ray Detection and Imaging, *ACS Appl. Mater. Interfaces*, 2024, **16**, 19068–19080.
45 M. Spahn, Flat detectors and their clinical applications, *Eur. Radiol.*, 2005, **15**, 1934–1947.
46 Q. Peng, Y. Si, J. Yuan, Q. Yang, Z. Gao, Y. Liu, Z. Wang, K. Li, S. Zang and B. Zhong Tang, High Performance Dynamic X–ray Flexible Imaging Realized Using a Copper Iodide Cluster–Based MOF Microcrystal Scintillator, *Angew. Chem., Int. Ed.*, 2023, e202308194.
47 H. Lu, X. Xu, Y. Li, G. Feng, J. Yang, X. Huang, Q. Luo, S. Wang and S. Wu, Heterovalent Co–Doped $LiLuF_4$ Composite Flexible Films as Persistent Luminescence Scintillator for X–Ray High–Resolution Extension Imaging, *Adv. Opt. Mater.*, 2024, 2303134.